ACS OMEGA

Article

Cite This: ACS Omega 2019, 4, 9262−9270

http://pubs.acs.org/journal/acsodf

Electrochemistry of Sputtered Hematite Photoanodes: A Comparison of Metallic DC versus Reactive RF Sputtering

Rochan Sinha,[†] Reinoud Lavrijsen,[‡] Marcel A. Verheijen,[‡] Erwin Zoethout,[†] Han Genuit,[†] Mauritius C. M. van de Sanden,[†,‡] and Anja Bieberle-Hütter*[,†]

[†]Dutch Institute for Fundamental Energy Research (DIFFER), PO Box 6336, 5600 HH Eindhoven, The Netherlands

[‡]Department of Applied Physics, Eindhoven University of Technology (TU/e), PO Box 513, 5600 MB Eindhoven, The Netherlands

Supporting Information

ABSTRACT: The water splitting activity of hematite is sensitive to the film processing parameters due to limiting factors such as a short hole diffusion length, slow oxygen evolution kinetics, and poor light absorptivity. In this work, we use direct current (DC) magnetron sputtering as a fast and cost-effective route to deposit metallic iron thin films, which are annealed in air to obtain well-adhering hematite thin films on F:SnO_2-coated glass substrates. These films are compared to annealed hematite films, which are deposited by reactive radio frequency (RF) magnetron sputtering, which is usually used for depositing metal oxide thin films, but displays an order of magnitude lower deposition rate. We find that DC sputtered films have much higher photoelectrochemical activity than reactive RF sputtered films. We show that this is related to differences in the morphology and surface composition of the films as a result of the different processing parameters. This in turn results in faster oxygen evolution kinetics and lower surface and bulk recombination effects. Thus, fabricating hematite thin films by fast and cost-efficient metallic iron deposition using DC magnetron sputtering is shown to be a valid and industrially relevant route for hematite photoanode fabrication.

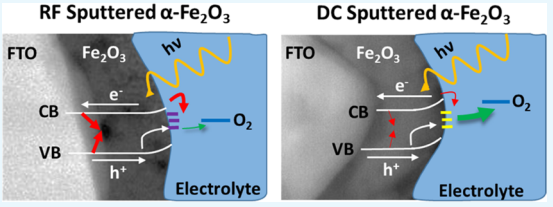

INTRODUCTION

Photoelectrochemical (PEC) water splitting has emerged as an attractive route for environmentally friendly generation of chemical fuels, also known as "solar fuels".[1] The appeal of this strategy arises due to the need for an efficient, large-scale storage of solar energy to fulfill the aim of a future low-carbon energy economy. However, to compete with other hydrogen generation techniques, such as methane steam reforming and electrolysis of water, PEC water splitting has to be made more efficient. The main reason for the limited efficiency is the four-electron oxygen evolution reaction (OER), which is kinetically challenging compared to the two-electron hydrogen evolution reaction (HER). Thus, development of efficient, stable, inexpensive, and abundant photoanodes that show high O_2 production is a significant bottleneck for developing a viable PEC system.[2−4]

Since the first demonstration of an operating PEC cell in 1972 utilizing TiO_2,[5] many other materials have been studied for their suitability as a photoanode. Of these, hematite (α-Fe_2O_3) remains one of the most widely studied materials for oxygen evolution reaction due to an optimum band gap (2−2.2 eV), excellent chemical stability, nontoxicity, abundance, and low cost.[4,6−8] The band gap of hematite ideally provides a theoretical solar-to-hydrogen (STH) efficiency of 12−16%.[9] Yet, the highest reported experimental STH efficiency for a hematite-based device is 3.4% in tandem with a $CH_3NH_3PbI_3$ perovskite solar cell.[10] This discrepancy in efficiency stems from the intrinsic material properties of hematite, such as poor light absorptivity due to an indirect band gap transition, short minority carrier lifetime (10 ps), and low minority charge carrier mobility (0.2 $cm^2\ V^{-1}\ s^{-1}$), leading to a short hole diffusion length of ca. 2−4 nm.[4,11] This leads to a large mismatch in the requirements for the film thickness, with around 400 nm required for complete light absorption (for light with a wavelength below 700 nm)[12,13] on the one hand, and less than 20 nm for efficient hole collection[4] on the other hand. Nanostructuring of hematite improves the performance compared to planar thin films,[14] but also increases the complexity of understanding the effect of film deposition and processing parameters on the PEC activity. Thus, in this work, hematite thin films are used since they provide an ideal system to study the impact of processing parameters on physical and chemical properties, which are related to changes in the PEC processes during OER.

Various physical and chemical synthesis techniques have been used to obtain efficient hematite photoanodes, such as sputtering,[15−17] atmospheric pressure chemical vapor deposition (APCVD),[7] atomic layer deposition (ALD),[18] ultrasonic spray pyrolysis,[19] and hydrothermal synthesis.[20] In the case of sputtering, hematite films are usually deposited either from a ceramic hematite target using a radio frequency (RF) power source[15,16] or from a metallic iron target in a reactive oxygen ambient using direct current (DC)[21] or RF[17] power sources. Sputtering from metal oxide targets and reactive sputtering

Received: November 30, 2018
Accepted: May 7, 2019
Published: May 28, 2019

DOI: 10.1021/acsomega.8b03349
ACS Omega 2019, 4, 9262−9270

processes are known to suffer from rather low deposition rates. DC magnetron sputtering from an iron target and subsequent annealing to iron oxide offer various advantages. Deposition rates of up to 3 Å s^{-1} are achieved in this work for the sputtered Fe films, which is an order of magnitude faster than typical RF sputtering processes from a ceramic target[15] or reactive RF sputtering from an iron target.[17] DC sputtering is also up to 3 orders of magnitude faster than ALD[22] while offering comparable control over deposition parameters. Thus, reproducible thin films with only minor variations in film properties between different batches can be obtained quickly and efficiently. Furthermore, DC sputtering is safer than chemical deposition processes, such as APCVD and spray pyrolysis, which use toxic precursors. Thus, DC magnetron sputtering offers a safe, cost-effective, and scalable deposition process for thin-film fabrication at an industrial scale.

In this work, we therefore use DC magnetron sputtering to deposit Fe thin films and transform them by subsequent annealing to hematite. We compare the PEC behavior of the DC sputtered films to hematite layers obtained by reactive RF sputtering, which is the standard method of fabricating metal oxide thin films, but is a much slower process as discussed above. Extensive physical and electrochemical characterization of these thin films allows us to relate the variation in the physicochemical properties as a result of changes in the sputtering process to the differences in the PEC activity.

RESULTS AND DISCUSSION

Structural Properties. Pure hematite phase is identified from the structural characterization of both the DC and RF sputtered thin films after annealing by grazing incidence X-ray diffraction (GI-XRD)[15,21] (Figure 1). Both films are

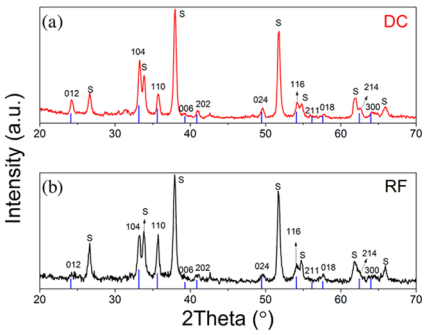

Figure 1. GI-XRD diffractograms of (a) DC and (b) RF sputtered hematite thin films after annealing. Peaks corresponding to the different crystallographic orientations for α-Fe_2O_3 (ICDD catalog number: 33-064) are represented by blue lines in the spectra and are labeled. The peaks corresponding to the FTO substrate are represented as "S" in the spectra.

polycrystalline in nature, but differences in the crystallographic orientation in the DC and RF films are seen. While the ratio of the (110) peak to the (104) peak of unoriented, polycrystalline hematite (ICDD catalogue number: 33-0664) is 1.429, it is seen to be 2.168 for the DC film and 0.98 for the RF film. This indicates a preferential growth of the hematite grains in the [104] direction for DC and in the [110] direction for RF sputtered films. It is known from the literature[16] that the electron mobility in hematite films is highly anisotropic and the mobility along the (001) basal plane is up to 4 orders of magnitude higher than in the perpendicular planes. This would suggest that the RF film with a higher (110) peak intensity will have a higher conductivity in the direction normal to the film compared to the DC film. This should help facilitate the charge carrier transport between the hematite−electrolyte interface and the FTO substrate in the RF film. It should be noted that in grazing incidence configuration, the preferred orientation for grains at angles equivalent to the incident angle (0.5° in our case) is determined. Hence, the texture of the film nearly parallel to the film surface is observed, but a quantitative analysis of the overall texture of the hematite thin film is not possible with this technique.

Thin-Film Morphology. The top-view morphologies of a DC sputtered 20 nm thick iron film and an RF sputtered 50 nm thick iron oxide film before annealing are illustrated in Figure 2a,b, respectively. Both DC and RF films look similar

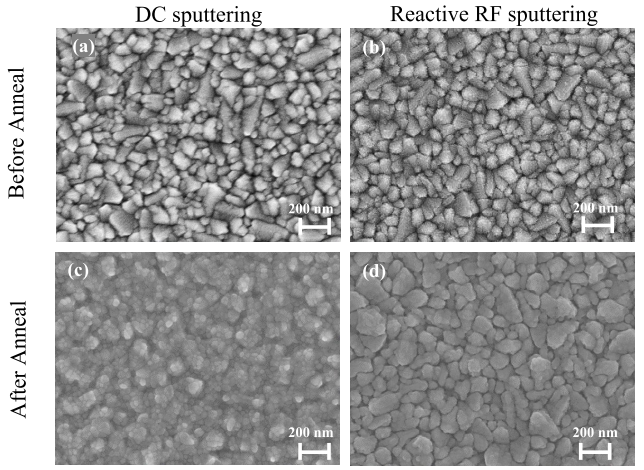

Figure 2. Top-view SEM images of (a) DC and (b) RF sputtered films before annealing and (c) DC and (d) RF sputtered films after annealing in air.

prior to annealing, showing a rough morphology similar to that of the underlying FTO (see Figure S1a in the Supporting Information). In both the cases, loosely packed grains are observed with large variation in both shape and size (40−200 nm).

After annealing, the DC and RF films demonstrate different morphologies. The DC film (Figure 2c), which converts from iron to hematite, undergoes a dramatic change in morphology. The film shows closely packed grains of 30−50 nm size with no voids between the grains and an underlying, large-scale morphology due to the FTO substrate. In contrast, the RF film (Figure 2d), which was already deposited as iron oxide (see Figure S2 in the Supporting Information), displays only minor variations in its morphology with slight coarsening of grains as well as disappearance of smaller (<50 nm) grains. The grains are still loosely packed with voids present between them.

The effect of the different sputtering techniques on the morphology of the thin films is further explored with cross-sectional high-angle annular dark-field scanning transmission electron microscopy (HAADF-STEM) (Figure 3). The DC film (Figure 3a) has a thickness of 40 ± 4 nm after annealing (see also Figure S1d). Hence, the thickness increases by 100%, which is due to the uptake of oxygen during annealing and the difference in density between Fe (7.86 g cm^{-3}) and α-Fe_2O_3 (5.26 g cm^{-3}). The DC film consists of closely packed grains grown on top of the FTO layer, as seen in the top-view SEM

DOI: 10.1021/acsomega.8b03349
ACS Omega 2019, 4, 9262−9270

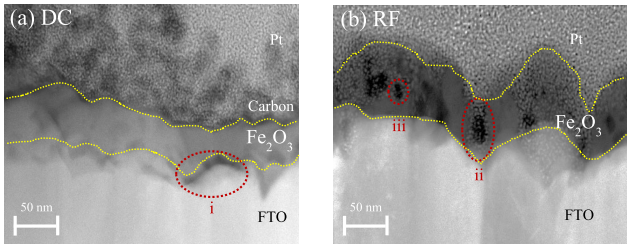

Figure 3. HAADF-STEM images of the (a) DC and (b) RF sputtered iron oxide thin films. All images were taken after annealing in air at 645 °C for 10 min. Pt and C layers were deposited using EBID to protect the iron oxide layer during sample preparation for TEM analysis. The yellow dotted lines are added as visual guidelines to demarcate the Fe_2O_3 layer. The red dotted circles indicate pinholes and voids.

image (Figure 2c). The grain sizes are similar to the film thickness and extend through the entire thickness of the film. Furthermore, voids are observed at some positions at the interface between hematite and FTO (marked "i" in Figure 3a), which is attributed to the roughness of the FTO layer.

On the other hand, the thickness of the RF sputtered α-Fe_2O_3 film does not change during annealing, having a final thickness of 47 ± 6 nm (Figures 3b and S1e), which is similar to the sputtered thickness. The discontinuous hematite layer grows as separate grains on top of the FTO grains and are separated by large pinholes (marked "ii" in Figure 3b). Furthermore, the TEM images show the presence of voids within the hematite grains themselves, which could not be observed by SEM imaging (marked "iii" in Figure 3b).

To understand the formation of these voids within the grains of the RF film, the changes occurring in the film morphology and crystal structure during annealing were studied (see Figures S1b,c and S2, respectively). From Figure S1b (which is a higher-magnification image of the RF film shown in Figure 2b), we observe that the RF film is sputtered as grains of size 40−200 nm. However, each grain consists of smaller nucleates of size 5−10 nm. After annealing, these nucleates grow and merge, leading to the formation of smoother grains, as observed in Figures S1c and 2d. Thus, one factor behind the formation of the voids is the merging of these nucleates when the RF film is annealed.

Another factor is the change in the hematite crystal structure on annealing, as shown in the XRD spectra in Figure S2. The peaks corresponding to the (104) and (110) orientation of the reactive RF sputtered hematite are observed to increase in intensity and decrease in the full width at half-maximum (FWHM). The increase in peak intensity is attributed to increased crystallinity of the film, while reduced FWHM values represent an increase in the crystallite size (also observed as the coarsening of the grains in Figure S1c). Furthermore, a shift of the hematite peaks to higher 2θ values is observed. The shift in the peak position occurs due to a change in the lattice constants of the hematite crystal structure. Hematite crystallizes in a rhombohedral corundum structure[23] and has a hexagonal unit cell with lattice constants "a" and "c". Annealing leads to a reduction in these lattice constants (see the Supporting Information), which could also lead to the coalescence of vacancies within the thin film and hence the formation of the voids. Evidently, the manner in which the hematite film growth occurs during reactive RF sputtering and its evolution during annealing lead to the formation of voids within the RF thin film.

Surface Composition. The surface compositions of the DC and RF sputtered hematite films were measured and analyzed by XPS (Figure 4). The fitting of the O 1s spectra for the DC and the RF films results in three peaks. The peak at 530 ± 0.15 eV is assigned to hematite lattice oxygen.[24] The second peak at 531.6 ± 0.1 eV is related to either hydroxyl species (OH^-) or oxygen vacancies ($V_o^{\cdot\cdot}$) at the surface.[25] The third peak at 532.6 ± 0.1 eV is attributed to adsorbed organic compounds, such as CO and CHO.[26] The peak intensity ratio of the O lattice peak and the OH^-/ $V_o^{\cdot\cdot}$ peak for the RF film was found to be 2.6 times lower compared to the DC film. These findings prove that the surface composition for hematite thin films varies depending on the sputtering route, with the RF film exhibiting a higher amount of either hydroxyl species or oxygen vacancies at the surface.

This observation is supported by the peak fitting results of the Fe $2p_{3/2}$ spectra (Figure S3) using the XPS parameters for α-Fe_2O_3, as proposed by Biesinger et al.[25] It is observed that the fitting for the DC film is better than that for the RF film based on the standard deviation values. However, a deviation of the fit from the spectra is seen in the peak fitting at lower binding energies (709−710 eV) and is especially pronounced for the RF film. This is attributed to the presence of another species at the surface, such as a defective oxide (due to oxygen vacancies) or an oxy-hydroxide species. From the O 1s spectra, it is evident that the aforementioned species are present for both films but in larger quantities at the surface of the RF film compared to the DC film. Quantification of the exact type and amount of mixed species present at the film surface by fitting of the Fe $2p_{3/2}$ spectra is complicated due to spectral overlap,

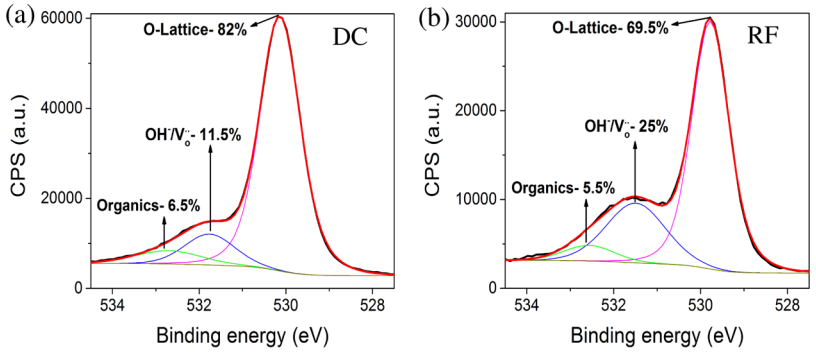

Figure 4. O 1s peak spectra and identified peak fits for (a) DC and (b) RF films. The black line is the measured spectrum, and the red line is the fitted curve; the magenta, blue, and green lines represent the individual peak fits. Peak fitting parameters are obtained from Beisinger et al.[23]

DOI: 10.1021/acsomega.8b03349
ACS Omega 2019, 4, 9262−9270

resulting in a larger degree of fitting error and, as such, is beyond the scope of this article.

Optical Properties. The optical absorption coefficient and band gap calculation for the DC and RF thin films are illustrated in Figure S4a,b, respectively. The absorption coefficient is calculated by normalizing the absorption spectra to the film thickness obtained from cross-sectional HAADF-STEM (Figure 3). RF films have a lower absorption coefficient in the entire wavelength range compared to DC films. This is related to the presence of voids and pinholes in the RF film, thus leading to less material that can absorb light. The indirect optical band gap is 2.1 eV for both the DC and RF films, which is similar to literature values.[4,6]

Photoelectrochemical Behavior. Figure 5 shows the current density versus applied potential (J–V) characteristics

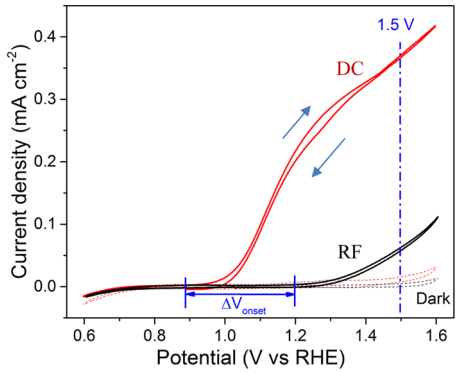

Figure 5. Current density versus applied potential (J–V) curves for DC (red) and RF (black) thin films annealed in air at 645 °C for 10 min. All measurements are done in 1 M NaOH in the dark (dotted lines) or under an illumination intensity of 100 mW cm^{-2} (solid lines). The arrows represent the direction of the CV cycle and is the same for all measurements.

of the DC and RF thin films annealed in air at 645 °C. The effect of varying annealing temperatures on the PEC behavior of the DC and RF films is summarized in Figure S5 in the Supporting Information. Figure 5 shows that the dark current (dotted lines) for both the DC and RF sputtered film remains negligible until 1.5 V versus RHE. The onset potential, V_{onset}, for the DC film is 0.88 V versus RHE, compared to the V_{onset} of 1.22 V versus RHE observed for the RF film. A higher onset potential (ΔV_{onset}) is related to slower OER kinetics and higher recombination in the RF film; this is discussed in detail in the next sections.

The DC film demonstrates a photocurrent of 0.36 mA cm^{-2} at 1.5 V versus RHE, which is 6 times higher than the photocurrent of the RF film at the same potential (0.06 mA cm^{-2}). The photocurrent of the DC film achieved herein is comparable to other bare, unmodified hematite thin films of 40–50 nm thickness prepared by various methods, such as sputtering or ALD.[16,18,27] However, it is lower than the hematite layer deposited by Jia et al. by RF sputtering from a ceramic hematite target (1.3 mA cm^{-2} at 1.5 V versus RHE).[15] The higher performance of the hematite films deposited by Jia et al. is most probably related to less physical defects in the bulk of the film. It should be noted, nevertheless, that the deposition rate in the paper by Jia et al. was only 0.14 Å s^{-1}, whereas the DC sputtered thin films in our study were deposited with a rate of 2.27 Å s^{-1}; this is 15 times faster.

Electrochemical Impedance Spectroscopy (EIS). To study the dynamics of the charge transfer and recombination processes occurring in the DC and RF films, EIS measurements were performed between 0.8 and 1.6 V versus RHE. Representative impedance spectra in the form of Nyquist plots are shown in Figure 6a for DC and RF films at 1.2 V versus RHE, respectively. Two main features are observed: A high-frequency arc with a relaxation frequency between 1000 and 5000 Hz (denoted by the green ★), which is characteristic for bulk processes in the semiconductor,[18] and a low-frequency arc at relaxation frequencies between 1 and 10 Hz (denoted by the magenta ◆), which is attributed to charge transfer processes related to the OER at the semiconductor–liquid interface.[28]

To gain a quantitative understanding of the features observed in the EIS spectra, the data were fitted with the equivalent circuit model (ECM) proposed by Klahr et al.[18] for hematite thin films. This model assumes that the OER occurs via surface states present at the hematite–electrolyte interface. Various studies have shown the existence of such surface states, as summarized by Zandi et al.,[6] and have also been recently observed directly by in operando ATR-FTIR studies.[29] The data were also fitted to other ECM models suggested in the literature, such as the Le Formal et al.[30] model, which states that the OER takes place via direct transfer from the valence band and the surface states only act as recombination centers. Fitting with the 2-R-CPE models as proposed by Lopes et al.[28] was also performed, which takes into account the Helmholtz layer capacitance (assuming it as a value similar to the space-charge layer capacitance). However, the best fit (lowest χ^2 value) and most realistic ECM component values were obtained for the Klahr model.

The ECM (Figure 6b) consists of the contact resistance, R_s; the capacitance of the space-charge layer in the hematite, C_{bulk}; the resistance associated with the charge recombination at the surface states, R_{trap}; the chemical capacitance associated with the density of charge carriers trapped at the surface states, C_{ss}; and the resistance associated with the charge transfer from the surface states to the electrolyte during the OER, R_{ss}. All of the fitting results are listed in Table S1 in the Supporting Information. Constant phase elements (CPE) are used in the ECM due to nonideal dielectric behavior of the hematite thin films. The quality of fit (denoted by χ^2) of the impedance spectra using an ECM with CPEs was 2 orders of magnitude better than with pure capacitors. The relation between capacitance and CPE fitting parameters is[31]

$$C = T^{1/p} \times R_{eff}^{(1-p)/p} \quad (1)$$

where T is the capacitance fitting parameter (F s^{p-1} cm^{-2}), p is the constant phase exponent ($0 < p < 1$), $R_{eff} = \frac{R_s \times R_{trap}}{R_s + R_{trap}}$ for CPE_{bulk} (assuming surface distribution of time constants),[32] and $R_{eff} = R_{ss}$ for CPE_{ss} (assuming normal distribution of time constants).[31]

Figure 6c shows the R_{trap} values for the DC and RF films between 0.8 and 1.6 V vs RHE. The R_{trap} values are approximately 4–5 times higher for the RF film compared to the DC film below 1.5 V versus RHE. This points to faster charge recombination at the surface states for the RF film and is one of the reasons for its lower PEC activity.

To study the charge transfer kinetics from the surface states to the electrolyte, the charge transfer resistance (R_{ss}) and surface state capacitance (C_{ss}) values for the two films are analyzed (Figures 6d,e). For the DC film (Figure 6d), the

DOI: 10.1021/acsomega.8b03349
ACS Omega 2019, 4, 9262–9270

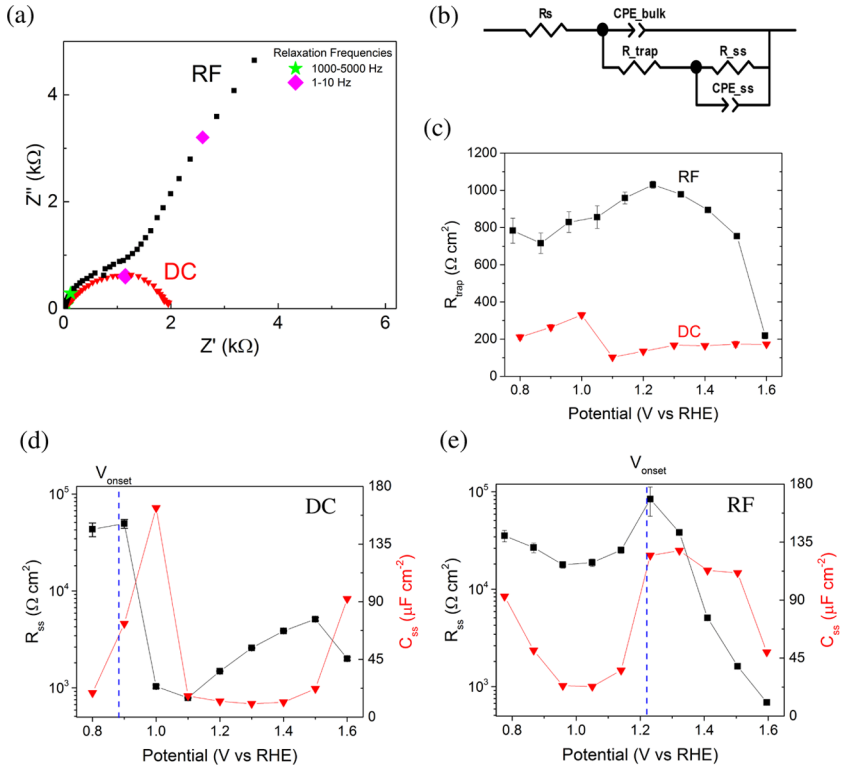

Figure 6. (a) Nyquist plot at 1.2 V versus RHE for the DC (red ▼) and RF (■) thin films, respectively. EIS was performed in the frequency range of 1 MHz to 0.1 Hz under an illumination intensity of 100 mW cm^{-2}. The star symbols (green ★) and diamond symbols (pink ◆) represent the relaxation frequencies for the bulk and interface processes, respectively. (b) Equivalent circuit model (ECM) used for fitting of the EIS data. (c) Surface recombination resistance (R_{trap}) for DC and RF films obtained from ECM fitting between 0.8 and 1.6 V versus RHE; (d, e) Charge transfer resistances R_{ss} (■) and surface state capacitances C_{ss} (red ▼) from ECM fitting between 0.8 and 1.6 V versus RHE for DC and RF films, respectively.

charge transfer resistance (R_{ss}) shows a decrease of more than 1 order of magnitude as the potential increases above V_{onset} of 0.88 V versus RHE (denoted by the dotted line) and then increases at more anodic potentials. This decrease in the charge transfer resistance is followed by a concomitant increase in the surface state capacitance (C_{ss}), which has a very low value below the onset potential, V_{onset}. It increases swiftly as V_{onset} is reached, with a maximum at 1 V (V_{onset} + 220 mV) and then declines rapidly at more anodic potentials.

These observations are explained by the fact that below V_{onset}, the holes trapped at the surface states do not have enough energy to initiate OER. Thus, as the potential increases, the holes accumulate at the surface states, leading to a peak in the C_{ss} value close to V_{onset}. Above V_{onset}, R_{ss} drops, since there is enough overpotential for OER to take place via the surface states, and since the holes are now consumed, the C_{ss} value decreases. This behavior of the C_{ss} and R_{ss} values for the DC film is a clear indication that the water oxidation takes place via surface states, as predicted theoretically by Bertoluzzi et al.[33] and also observed experimentally in the literature.[18,27,34]

For the RF film (Figure 6e), a different trend with potential for both R_{ss} and C_{ss} values is observed. This is due to the highly anodic V_{onset} for RF film with a value of 1.22 V versus RHE. C_{ss} increases above 1.1 V and reaches a maximum at 1.3 V (80 mV above V_{onset}). However, the broad peak of the C_{ss} exhibits high values up to 1.5 V, unlike the sharp C_{ss} peak observed at 1 V for the DC film. R_{ss} first increases up to just above V_{onset} and then starts to decrease, but the slope is less pronounced compared to the DC films. In addition, the higher R_{ss} values for RF films below 1.3 V versus RHE suggest slower OER kinetics. These different trends for the R_{ss} and C_{ss} for the DC and RF films and the much higher V_{onset} for the latter are attributed to different types of surface states for the two films. The difference in the surface states is related to higher peak intensity corresponding to the presence of either hydroxyl species (OH^-) or oxygen vacancies ($V_o^{\cdot\cdot}$), as observed in the O1s spectra for the RF film (Figure 4), which can lead to lower OER activity in hematite thin films.[35,36]

Intensity-Modulated Photocurrent Spectroscopy (IMPS). IMPS[37,38] was used to further determine the rate constants of the surface state recombination and charge transfer processes. In this technique, the frequency response of the photocurrent is measured with respect to the sinusoidal modulation of the light source. The IMPS response is plotted in a Nyquist plot with the complex photocurrent as a function of the light modulation frequency (see Figure S6). The high-frequency intercept (HFI) with the real photocurrent axis corresponds to the hole current (j_{hole}), since the recombination rate is much lower than the rate at which the hole concentration changes. The low-frequency intercept (LFI) represents the steady-state photocurrent (j_{photo}), which is the fraction of the hole at the surface that undergoes charge transfer to the electrolyte. The ratio of LFI to HFI gives the charge transfer efficiency (η_t)[39]

$$\eta_t = \frac{\text{low freq. intercept (LFI)}}{\text{high freq. intercept (HFI)}} = \frac{j_{photo}}{j_{hole}} = \frac{k_t}{k_t + k_r} \quad (2)$$

DOI: 10.1021/acsomega.8b03349
ACS Omega 2019, 4, 9262−9270

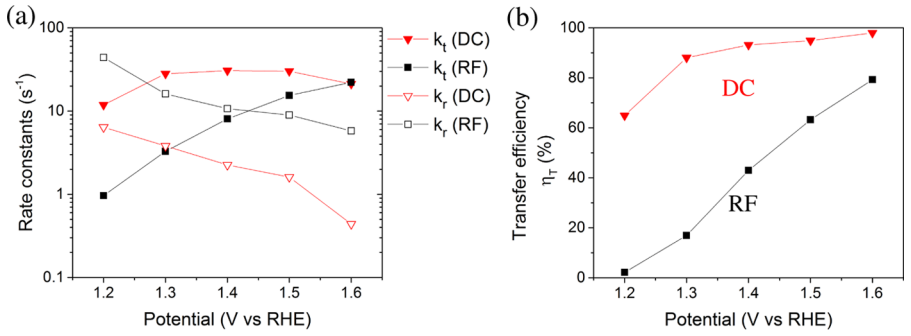

Figure 7. (a) Charge transfer rate constants (k_t: solid symbols) and surface recombination rate constant (k_r: open symbols) for DC and RF films between 1.2 and 1.6 V versus RHE. (b) Charge transfer efficiency (η_t) for DC (red symbol) and RF (black symbol) thin films between 1.2 and 1.6 V versus RHE. All measurements were done in 1 M NaOH under illumination from a 405 nm LED (ThorLabs) with an illumination intensity of 22 mW cm^{-2}.

where k_t is the charge transfer rate constant and k_r is the surface recombination rate constant. Furthermore, the radial frequency at the apex of the semicircle (ω_{max}) in the upper quadrant of the plot is given by the combined rate of charge transfer and surface recombination ($k_t + k_r$).[37,40]

Figure 7 shows the rate constants for charge transfer (k_t) and surface recombination (k_r) and the charge transfer efficiency (η_t) obtained for DC and RF films between 1.2 and 1.6 V versus RHE. The values and trends for the obtained parameters lie within the range expected for plain hematite films and are in good agreement with previously reported IMPS analyses by Peter et al.[39] and Thorne et al.[41]

Figure 7a shows that the charge transfer rate constant k_t (solid symbols) is higher for the DC film at all potentials below 1.6 V vs RHE, pointing to faster OER kinetics compared to the RF film. Furthermore, the k_t value for the DC film saturates around 30 s^{-1}, whereas it increases almost linearly for the RF film. This can be understood from the fact that as the bias is increased, the RF film with poor OER activity shows a much larger improvement in charge transfer kinetics. This also explains why photocurrent saturation is observed for the DC film, but not for the RF film at potentials above 1.2 V versus RHE in the $J-V$ curve (Figure 5).

Furthermore, the surface state recombination rate constant (k_r) (open symbols in Figure 7a) is up to an order of magnitude higher for the RF film in the entire potential window compared to the DC film. This confirms that there is higher surface state recombination in the RF film, which is also observed from the higher R_{trap} values as found by EIS for the RF film (Figure 6c). Moreover, value of k_r decreases for both DC and RF films with increasing potential, which is explained by the more efficient charge carrier separation as the result of increase in band bending with applied potential. The difference in magnitude- and potential-dependent behaviors of k_t and k_r for the DC and RF films occurs as a result of difference in the surface states for the DC and RF films, as observed from XPS, with the latter showing a higher concentration of surface species (either hydroxyl group or oxygen vacancies), which have been shown to reduce the charge transfer kinetics in hematite.

The effect of the large differences in the k_t and k_r values for the DC and RF films is clearly reflected in the charge transfer efficiency curve (Figure 7b). The DC film has a charge transfer efficiency greater than 60% at 1.2 V and almost reaches 100% efficiency at 1.6 V versus RHE. The RF film, in contrast, has a minimal efficiency at 1.2 V, concomitant with the very high V_{onset} of 1.22 V versus RHE, while the efficiency at 1.6 V is still below 80%. This explains the much higher photocurrent and lower V_{onset} for the DC films and reinforces the observations from the EIS showing the faster OER kinetics and lower surface state recombination for the DC film compared to the RF film, which points to differences in the surface states for the two films.

Hole Scavenger Measurements. Apart from surface state recombination and slow charge transfer kinetics, another important factor affecting the PEC activity of hematite thin films is the bulk recombination. This was studied by performing hole scavenger measurements in a 1 M NaOH + 0.1 M H_2O_2 electrolyte. Hole scavengers remove the effect of surface recombination and slow OER kinetics and ensure that the photocurrent is solely limited by bulk recombination within the hematite layer.[42] The photocurrents obtained for DC and RF films annealed at 645 °C are shown in Figure 8

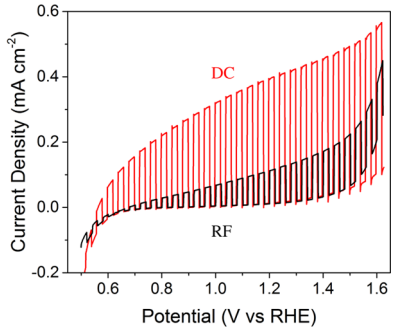

Figure 8. Chopped-light measurements performed for the DC (red) and RF (black) thin films (annealed at 645 °C) in 1 M NaOH + 0.1 M H_2O_2 electrolyte. The light was chopped with a frequency of 0.5 Hz. The illumination intensity was 100 mW cm^{-2}.

(the corresponding hole scavenger measurements for films annealed at 800 °C are shown in Figure S8). It is observed that the photocurrent for the DC film is much higher than that for the RF film in the entire potential range. This confirms that DC films have lower bulk recombination than RF films, which is attributed to the presence of voids in the RF film and contributes to its poor PEC activity.

SUMMARY AND CONCLUSIONS

We used two sputtering routes, namely, DC and reactive RF sputtering, to fabricate Fe and FeO_x thin films, respectively. All thin films were annealed in air after deposition to obtain 40–

DOI: 10.1021/acsomega.8b03349
ACS Omega 2019, 4, 9262−9270

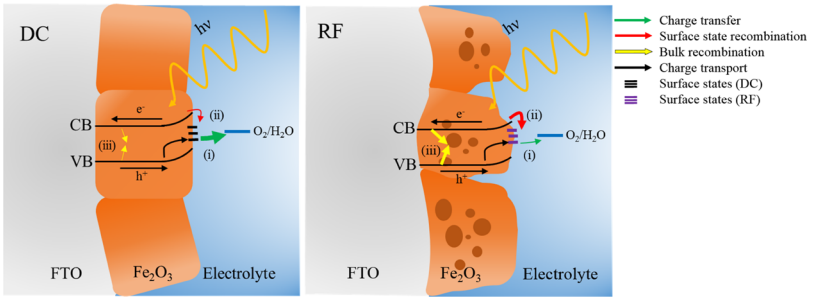

Figure 9. Schematic illustrating the differences in the (i) charge transfer kinetics, (ii) surface state recombination rate, and (iii) bulk recombination rate of DC and RF hematite thin films and the relation to their physicochemical properties. The black arrow represents hole transport from the valence band to surface states. The thick lines represent the major process, while the thin lines represent minor processes occurring in the thin films.

50 nm thick hematite films. The DC sputtered film had a 6 times higher photocurrent at 1.5 V versus RHE as well as a lower onset potential (0.88 V versus RHE) than the RF sputtered film (1.22 V versus RHE).

The schematic shown in Figure 9 summarizes the main factors contributing to the better PEC activity of DC sputtered thin films and their relation to the physicochemical properties of the DC and RF sputtered hematite films. The first factor is the faster charge transfer kinetics (denoted by (i) in the schematic) in the DC film compared to the RF film. This is illustrated by the green arrows: the thicker the arrow, the faster the charge transfer kinetics. Another factor is the lower recombination rate of the electrons with the holes trapped at the surface states (denoted by (ii)) in the DC film compared to the RF film. This process is represented by red arrows; the slower the recombination, the thinner the arrow. The differences in charge transfer kinetics and surface state recombination rate are due to the differences in the type of surface states for the DC and reactive RF sputtered films. This is related to the higher peak intensity corresponding to either hydroxyl species (OH^-) or defective oxide ($V_o^{\cdot\cdot}$) at the surface of the RF film.

The difference in concentration of the hydroxyl species or defective oxide on the surface of the DC and RF films could be related to the difference in the crystallographic orientation at the surface due to changes in the preferential growth of the grains for the two films. Finally, the densely packed, homogeneous grain structure of the DC films leads to lower bulk recombination (denoted by (iii)) compared to the RF film, as represented by the yellow arrows; the thinner arrows represent lower bulk recombination. This is related to the presence of voids within the grains of the RF film, which occur as a result of the distinctive iron oxide growth process during the reactive RF sputtering process and the subsequent annealing step.

In conclusion, DC magnetron sputtering was used to deposit metallic Fe films on FTO-glass substrates, which after annealing led to well-adhered and stable hematite films exhibiting good PEC activity. These films were compared to hematite films obtained by reactive RF sputtering with an order of magnitude lower deposition rate. On subsequent annealing of the RF films, they demonstrated significantly lower PEC activity. A detailed study of the physicochemical and photoelectrochemical properties was performed, and the relation between the film properties and PEC behavior was established. Thus, DC sputtering as a fast, low-cost, and scalable method for depositing photoelectrodes was demonstrated and provides superior films compared to reactive RF sputtering.

EXPERIMENTAL SECTION

Thin-Film Preparation. Iron and iron oxide thin films were deposited by DC and reactive RF magnetron sputtering, respectively, on glass substrates (2 mm thick) coated with an F:SnO_2 (FTO) conducting layer of approximately 200 nm thickness and 15 Ω sq^{-1} sheet resistivity (MTI TEC15). The dimensions of the FTO-coated glass substrates are 2.5 cm × 2.5 cm. The FTO substrates were cleaned following the method proposed by Malviya et al.[43] A sputter tool from Kurt J. Lesker was used with a base pressure <10^{-7} mbar and a target−substrate distance of 95 mm. Both DC and RF magnetron sputtering experiments were carried out at room temperature using a 2″ Fe sputter target. For DC sputtering, an Ar flow of 7 sccm at a deposition pressure of 1.25 × 10^{-2} mbar and power of 100 W was used. The films were sputtered for 88 s with a sputter rate of 2.27 Å s^{-1} to obtain a Fe film with thickness of 20 nm. Reactive RF magnetron sputtering was performed with mixed Ar and O_2 flows of 7 and 2 sccm, respectively, with a deposition pressure of 1.4 × 10^{-2} mbar and a power of 200 W. Sputtering was performed for 1515 s at a sputter rate of 0.33 Å s^{-1} to obtain a 50 nm Fe_2O_3 layer. All films were annealed in air at a temperature of 645 °C for 10 min or 800 °C for 5 min to obtain crystalline hematite thin films. A ramp rate of 5 °C min^{-1} was applied to reach the desired annealing temperature.

Physicochemical Characterization. The top-view morphologies of the thin films were examined by field emission scanning electron microscopy (SEM) (Zeiss Sigma) with an in-lens detector and 5 kV accelerating voltage. High-angle annular dark-field scanning transmission electron microscopy (HAADF-STEM) of the thin-film cross sections was performed using a JEOL ARM200F TEM setup operated at 200 kV. TEM cross sections of the thin films were prepared using focused ion beam milling. Pt and carbon protective layers were deposited using ion-beam-induced deposition (IBID) and electron-beam-induced deposition (EBID) to preserve the thin-film structure during the milling process.

Structural characterization was performed using a Bruker D8 Eco X-ray diffractometer (XRD) with a Cu Kα (λ= 1.5406 Å) source and a Lynx-eye detector in a grazing incidence configuration (GI-XRD) at an incident angle of 0.5° and in the 2θ range of 20−80°. A Thermo Scientific Kα X-ray photoelectron spectroscopy (XPS) setup equipped with a monochromated Al Kα source ($h\nu$ = 1486.6 eV) was used for the chemical analysis. The binding energy was corrected with

DOI: 10.1021/acsomega.8b03349
ACS Omega 2019, 4, 9262−9270

respect to the adventitious carbon C 1s peak at 284.8 eV. Peak fitting was done using the Casa XPS software. The optical absorbance of the films was characterized with a PerkinElmer 1050 UV/vis/NIR spectrophotometer in the wavelength range of 300−900 nm.

Electrochemical Characterization. An in-house three-electrode electrochemical cell fitted with a quartz window was used for electrochemical characterization. An aqueous solution of 1 M NaOH was used as the electrolyte. For hole scavenger measurements, a 1 M NaOH + 0.1 M H_2O_2 electrolyte was used. A coiled Pt wire and a Ag/AgCl/Sat. KCl electrode (XR 300, Radiometer Analytical) were used as the counter electrode (CE) and reference electrode (RE), respectively. The geometric area of the working electrode exposed to the electrolyte was 0.785 cm^2. The potential of the electrode was controlled with a BioLogic SP-150 potentiostat. All potentials reported are versus RHE through the relation[2]

$$\Phi_{RHE} = \Phi_{Ag/AgCl} + \Phi^{\circ}_{Ag/AgCl\ vs\ RHE} + 0.059 \times pH \quad (3)$$

with $\Phi^{\circ}_{Ag/AgCl\ vs\ RHE}$ = 0.198 V versus RHE at 25 °C. Illumination was provided by an AM 1.5 class A solar simulator (LCS 100, Oriel Instruments) using a 100 W Xe lamp with a calibrated illumination intensity of 100 mW cm^{-2} at the sample position (Reference cell 91150 V, Newport). All measurements were done at potentials between 0.6 and 1.6 V versus RHE. Cyclic voltammetry measurements were performed at a scan rate of 20 mV s^{-1}. The onset potential was taken as the potential at which the first derivative of the photocurrent density with respect to the potential (dj/dV) achieved 10 times the value observed for the first derivative of the dark current measurement. This technique was adopted from Le Formal et al.[11] Transient photocurrent measurements were obtained by chopping the incident light with an externally controlled shutter at a rate of 0.5 s^{-1} while performing linear sweep voltammetry (LSV) at a scan rate of 10 mV s^{-1}.

Electrochemical impedance spectroscopy (EIS) was performed in a frequency range of 1 MHz to 0.1 Hz. The magnitude of the modulation signal applied to the potential was 10 mV. The potential at which the EIS scans were performed was increased stepwise by 0.1 V between 0.6 and 1.6 V versus RHE. Equivalent circuit fitting of the EIS images was performed using the ZView software. A Solartron ModuLab XM potentiostat with photoelectrochemical accessory was used for intensity-modulated photocurrent spectroscopy (IMPS) measurements. A 455 nm LED (ThorLabs) with an illumination intensity of 22 mW cm^{-2} was used as a light source. A 10% AC modulation intensity was used for the measurements in the frequency range of 50 kHz to 0.1 Hz. The electrochemical cell, RE, and CE were the same as those used for the other PEC measurements.

■ ASSOCIATED CONTENT

Supporting Information

The Supporting Information is available free of charge on the ACS Publications website at DOI: 10.1021/acsomega.8b03349.

Additional SEM images of bare FTO substrate; SEM and XRD spectra of reactive RF sputtered thin film before and after annealing; fitted Fe $2p_{3/2}$ spectra of DC and RF films; optical absorption coefficient and Tauc plot for DC and RF films; comparison of the average onset potential and photocurrent (at 1.23 and 1.5 V versus RHE) for both DC and RF films annealed at different temperatures; IMPS Nyquist plot of hematite thin film; ECM fitting values obtained by fitting of the impedance spectra for both DC and RF films between 0.6 and 1.6 V versus RHE; Mott−Schottky plot for DC and RF films with and without a hole scavenger; and chopped-light measurements with hole scavenger for DC and RF films annealed at 800 °C (PDF)

■ AUTHOR INFORMATION

Corresponding Author

*E-mail: a.bieberle@differ.nl.

ORCID

Rochan Sinha: 0000-0001-9389-205X

Anja Bieberle-Hütter: 0000-0001-8794-9312

Author Contributions

The manuscript was written through contribution of all authors. All authors have given approval to the final version of the manuscript.

Funding

FOM program number 147 "CO_2 neutral fuels" Solliance and the Dutch province of Noord-Brabant.

Notes

The authors declare no competing financial interest.

■ ACKNOWLEDGMENTS

Sinha, Bieberle-Hütter, and van de Sanden acknowledge the financial support from NWO (FOM program number 147 "CO_2 neutral fuels"). The authors thank Michail Tsampas, Aafke Bronneberg, and George Nikiforidis from DIFFER for their valuable input to the manuscript. Beatriz Barcones-Campos, Applied Physics, TU Eindhoven, is acknowledged for preparation of the TEM cross sections. NanoLab at TU Eindhoven is acknowledged for access to SEM and XPS. Solliance and the Dutch province of Noord-Brabant are acknowledged for funding the TEM facility.

■ REFERENCES

(1) Walter, M. G.; Warren, E. L.; McKone, J. R.; Boettcher, S. W.; Mi, Q.; Santori, E. A.; Lewis, N. S. Solar Water Splitting Cells. *Chem. Rev.* **2010**, *110*, 6446−6473.

(2) Krol, R. v. d.; Grätzel, M. *Photoelectrochemical Hydrogen Production*; Springer: New York, 2011.

(3) Chen, H. M.; Chen, C. K.; Liu, R.-S.; Zhang, L.; Zhang, J.; Wilkinson, D. P. Nano-Architecture and Material Designs for Water Splitting Photoelectrodes. *Chem. Soc. Rev.* **2012**, *41*, 5654−5671.

(4) Sivula, K.; Le Formal, F.; Grätzel, M. Solar Water Splitting: Progress Using Hematite (α-Fe_2O_3) Photoelectrodes. *ChemSusChem* **2011**, *4*, 432−449.

(5) Fujishima, A.; Honda, K. Electrochemical Photolysis of Water at a Semiconductor Electrode. *Nature* **1972**, *238*, 37.

(6) Zandi, O.; Hamann, T. W. The Potential versus Current State of Water Splitting with Hematite. *Phys. Chem. Chem. Phys.* **2015**, *17*, 22485−22503.

(7) Kay, A.; Cesar, I.; Grätzel, M. New Benchmark for Water Photooxidation by Nanostructured α-Fe_2O_3 Films. *J. Am. Chem. Soc.* **2006**, *128*, 15714−15721.

(8) Bora, D. K.; Braun, A.; Constable, E. C. "In Rust We Trust". Hematite - the Prospective Inorganic Backbone for Artificial Photosynthesis. *Energy Environ. Sci.* **2013**, *6*, 407.

(9) Murphy, A. B.; Barnes, P. R. F.; Randeniya, L. K.; Plumb, I. C.; Grey, I. E.; Horne, M. D.; Glasscock, J. A. Efficiency of Solar Water Splitting Using Semiconductor Electrodes. *Int. J. Hydrogen Energy* **2006**, *31*, 1999−2017.

DOI: 10.1021/acsomega.8b03349
ACS Omega 2019, 4, 9262−9270

(10) John, R. A.; Boix, P. P.; Yi, C.; Shi, C.; Scott, M. C.; Veldhuis, S. A.; Minor, A. M.; Zakeeruddin, S. M.; Wong, L. H.; et al. Atomically Altered Hematite for Highly Efficient Perovskite Tandem Water-Splitting Devices. *ChemSusChem* **2017**, *10*, 2449−2456.
(11) Le Formal, F.; Grätzel, M.; Sivula, K. Controlling Photoactivity in Ultrathin Hematite Films for Solar Water-Splitting. *Adv. Funct. Mater.* **2010**, *20*, 1099−1107.
(12) Itoh, K.; Bockris, J. O. M. Stacked Thin-Film Photoelectrode Using Iron Oxide. *J. Appl. Phys.* **1984**, *56*, 874−876.
(13) Kay, A.; Grave, D. A.; Malviya, K. D.; Ellis, D. S.; Dotan, H.; Rothschild, A. Wavelength Dependent Photocurrent of Hematite Photoanodes: Reassessing the Hole Collection Length. *J. Phys. Chem. C* **2017**, *121*, 28287−28292.
(14) Kim, J. Y.; Magesh, G.; Youn, D. H.; Jang, J.-W.; Kubota, J.; Domen, K.; Lee, J. S. Single-Crystalline, Wormlike Hematite Photoanodes for Efficient Solar Water Splitting. *Sci. Rep.* **2013**, *3*, No. 2681.
(15) Jia, L.; Harbauer, K.; Bogdanoff, P.; Herrmann-Geppert, I.; Ramírez, A.; van de Krol, R.; Fiechter, S. α-Fe_2O_3 Films for Photoelectrochemical Water Oxidation − Insights of Key Performance Parameters. *J. Mater. Chem. A* **2014**, *2*, 20196−20202.
(16) Kment, S.; Schmuki, P.; Hubicka, Z.; Machala, L.; Kirchgeorg, R.; Liu, N.; Wang, L.; Lee, K.; Olejnicek, J.; Cada, M.; et al. Photoanodes with Fully Controllable Texture: The Enhanced Water Splitting Efficiency of Thin Hematite Films Exhibiting Solely (110) Crystal Orientation. *ACS Nano* **2015**, *9*, 7113−7123.
(17) Hahn, N. T.; Ye, H.; Flaherty, D. W.; Bard, A. J.; Mullins, C. B. Reactive Ballistic Deposition of α-Fe_2O_3 Thin Films for Photoelectrochemical Water Oxidation. *ACS Nano* **2010**, *4*, 1977−1986.
(18) Klahr, B.; Gimenez, S.; Fabregat-Santiago, F.; Hamann, T.; Bisquert, J. Water Oxidation at Hematite Photoelectrodes: The Role of Surface States. *J. Am. Chem. Soc.* **2012**, *134*, 4294−4302.
(19) Duret, A.; Grätzel, M. Visible Light-Induced Water Oxidation on Mesoscopic α-Fe_2O_3 Films Made by Ultrasonic Spray Pyrolysis. *J. Phys. Chem. B* **2005**, *109*, 17184−17191.
(20) Vayssieres, L.; Beermann, N.; Lindquist, S. E.; Hagfeldt, A. Controlled Aqueous Chemical Growth of Oriented Three-Dimensional Crystalline Nanorod Arrays: Application to Iron(III) Oxides. *Chem. Mater.* **2001**, *13*, 233−235.
(21) Glasscock, J. A.; Barnes, P. R. F.; Plumb, I. C.; Savvides, N. Enhancement of Photoelectrochemical Hydrogen Production from Hematite Thin Films by the Introduction of Ti and Si. *J. Phys. Chem. C* **2007**, *111*, 16477−16488.
(22) Klahr, B. M.; Martinson, A. B. F.; Hamann, T. W. Photoelectrochemical Investigation of Ultrathin Film Iron Oxide Solar Cells Prepared by Atomic Layer Deposition. *Langmuir* **2011**, *27*, 461−468.
(23) Ketteler, G.; Weiss, W.; Ranke, W.; Schlögl, R. Bulk and Surface Phases of Iron Oxides in an Oxygen and Water Atmosphere at Low Pressure. *Phys. Chem. Chem. Phys.* **2001**, *3*, 1114−1122.
(24) Grosvenor, A. P.; Kobe, B. A.; Biesinger, M. C.; McIntyre, N. S. Investigation of Multiplet Splitting of Fe 2p XPS Spectra and Bonding in Iron Compounds. *Surf. Interface Anal.* **2004**, *36*, 1564−1574.
(25) Biesinger, M. C.; Payne, B. P.; Grosvenor, A. P.; Lau, L. W. M.; Gerson, A. R.; Smart, R. S. C. Resolving Surface Chemical States in XPS Analysis of First Row Transition Metals, Oxides and Hydroxides: Cr, Mn, Fe, Co and Ni. *Appl. Surf. Sci.* **2011**, *257*, 2717−2730.
(26) Grosvenor, A. P.; Kobe, B. A.; McIntyre, N. S. Examination of the Oxidation of Iron by Oxygen Using X-Ray Photoelectron Spectroscopy and QUASES. *Surf. Sci.* **2004**, *565*, 151−162.
(27) Wickman, B.; Bastos Fanta, A.; Burrows, A.; Hellman, A.; Wagner, J. B.; Iandolo, B. Iron Oxide Films Prepared by Rapid Thermal Processing for Solar Energy Conversion. *Sci. Rep.* **2017**, *7*, No. 40500.
(28) Lopes, T.; Andrade, L.; Le Formal, F.; Grätzel, M.; Sivula, K.; Mendes, A. Hematite Photoelectrodes for Water Splitting: Evaluation of the Role of Film Thickness by Impedance Spectroscopy. *Phys. Chem. Chem. Phys.* **2014**, *16*, 16515.
(29) Zandi, O.; Hamann, T. W. Determination of Photoelectrochemical Water Oxidation Intermediates on Hematite Electrode Surfaces Using Operando Infrared Spectroscopy. *Nat. Chem.* **2016**, *8*, 778−783.
(30) Le Formal, F.; Pendlebury, S. R.; Cornuz, M.; Tilley, S. D.; Grätzel, M.; Durrant, J. R. Back Electron−Hole Recombination in Hematite Photoanodes for Water Splitting. *J. Am. Chem. Soc.* **2014**, *136*, 2564−2574.
(31) Hirschorn, B.; Orazem, M. E.; Tribollet, B.; Vivier, V.; Frateur, I.; Musiani, M. Determination of Effective Capacitance and Film Thickness from Constant-Phase-Element Parameters. *Electrochim. Acta* **2010**, *55*, 6218−6227.
(32) Brug, G. J.; Eeden, A. L. G. V. D.; Sluyters-Rehbach, M.; Sluyters, J. H. The Analysis of Electrode Impedances Complicated by the Presence of a Constant Phase Element. *J. Electroanal. Chem. Interfacial Electrochem.* **1984**, *176*, 275−295.
(33) Bertoluzzi, L.; Bisquert, J. Equivalent Circuit of Electrons and Holes in Thin Semiconductor Films for Photoelectrochemical Water Splitting Applications. *J. Phys. Chem. Lett.* **2012**, *3*, 2517−2522.
(34) Iandolo, B.; Hellman, A. The Role of Surface States in the Oxygen Evolution Reaction on Hematite. *Angew. Chem., Int. Ed.* **2014**, *53*, 13404−13408.
(35) Hu, Y.; Boudoire, F.; Hermann-Geppert, I.; Bogdanoff, P.; Tsekouras, G.; Mun, B. S.; Fortunato, G.; Grätzel, M.; Braun, A. Molecular Origin and Electrochemical Influence of Capacitive Surface States on Iron Oxide Photoanodes. *J. Phys. Chem. C* **2016**, *120*, 3250−3258.
(36) Rioult, M.; Stanescu, D.; Fonda, E.; Barbier, A.; Magnan, H. Oxygen Vacancies Engineering of Iron Oxides Films for Solar Water Splitting. *J. Phys. Chem. C* **2016**, *120*, 7482−7490.
(37) Peter, L. Dynamic Aspects of Semiconductor Photoelectrochemistry. *Chem. Rev.* **1990**, *90*, 753−769.
(38) Ponomarev, E. A.; Peter, L. M. A Generalized Theory of Intensity Modulated Photocurrent Spectroscopy (IMPS). *J. Electroanal. Chem. Interfacial Electrochem.* **1995**, *396*, 219−226.
(39) Peter, L. M.; Wijayantha, K. G. U.; Tahir, A. A. Kinetics of Light-Driven Oxygen Evolution at α-Fe_2O_3 Electrodes. *Faraday Discuss.* **2012**, *155*, 309−322.
(40) Peter, L. M. Energetics and Kinetics of Light-Driven Oxygen Evolution at Semiconductor Electrodes: The Example of Hematite. *J. Solid State Electrochem.* **2013**, *17*, 315−326.
(41) Thorne, J. E.; Jang, J.-W.; Liu, E. Y.; Wang, D. Understanding the Origin of Photoelectrode Performance Enhancement by Probing Surface Kinetics. *Chem. Sci.* **2016**, *7*, 3347−3354.
(42) Dotan, H.; Sivula, K.; Grätzel, M.; Rothschild, A.; Warren, S. C. Probing the Photoelectrochemical Properties of Hematite (α-Fe_2O_3) Electrodes Using Hydrogen Peroxide as a Hole Scavenger. *Energy Environ. Sci.* **2011**, *4*, 958.
(43) Malviya, K. D.; Dotan, H.; Yoon, K. R.; Kima, I.-D.; Rothschild, A. Rigorous Substrate Cleaning Process for Reproducible Thin Film Hematite (α-Fe_2O_3) Photoanodes. *J. Mater. Res.* **2015**, 1−23.

DOI: 10.1021/acsomega.8b03349
ACS Omega 2019, 4, 9262−9270